Supplementary Materials: Groundwater Flow Modeling in Karst Aquifers: Coupling 3D Matrix and 1D Conduit Flow via Control Volume Isogeometric Analysis — Experimental Verification with a 3D Physical Model

Luka Malenica [1,*], Hrvoje Gotovac [1], Grgo Kamber [1], Srdjan Simunovic [2], Srikanth Allu [2], Vladimir Divic [1]

1. Introduction

The karst aquifers are characterized by the existence of the highly permeable conduit network embedded in the less permeable karst (rock) matrix. This duality of permeability results in different flow conditions and makes karst distinct from other aquifers and more difficult to model. For the purposes of the project: "Groundwater flow modeling in karst aquifers", a 3D karst flow model (Figure S1) was built in front of the Hydrotechnical Laboratory in Žrnovnica near Split.

The physical model is constructed as a concrete structure of total dimensions: 5.66 m x 2.95 m x 2.00 m. Two water reservoirs are used to regulate the piezometric water levels at the upstream and downstream end of the model. By establishing a difference in water levels, different flow gradients can be achieved. The space between the two tanks is filled with heterogeneous porous material and represents the matrix of the physical model. Within the matrix, the perforated plastic pipes are installed and used to simulate the karst conduits in which rapid turbulent flow occurs. On the top of the construction, there are installed sprinklers and shower heads for rainfall simulation. The model enables the measurement of discharges from both conduits and the matrix as well as hydraulic head distribution in the porous matrix.

Figure S1. Photography of the physical model.

2. Technical description

2.1. Karst conduits

There are three different pipes installed and labeled C1, C2 and C3 (Figures S2 and S3). Pipes C1 and C3 have diameter 0.0155 m, whereas pipe C2's diameter is 0.042 m. The dashed lines in Figure S2 represent the perforated parts of the pipes. For C1 and C3, the perforations are handmade by drilling holes of 3 mm diameter. The C1 has 80 perforation uniformly distributed along perforated length, while C3 has 4 x 13 perforations on 4 branches as shown in Figure S2. The C2 pipe is made of two parts: the first is unperforated PVC pipe, and the second is manufactured drainage pipe. The specified values of Manning coefficents are $n_M = 0.009$ m$^{1/3}$ s for C1 and C3 pipes, and $n_M = 0.015$ m$^{1/3}$ s for unperforated part of C2. The Manning coefficient for perforated part of C2 pipe was not specified; thus it needed numerical calibration. The perforated parts were wrapped into geotextile and installed inside fine quartz sand (see section 2.2) to prevent clogging of perforations. Table S1 reports the coordinates of points defining pipe geometries (according to Figures S2).

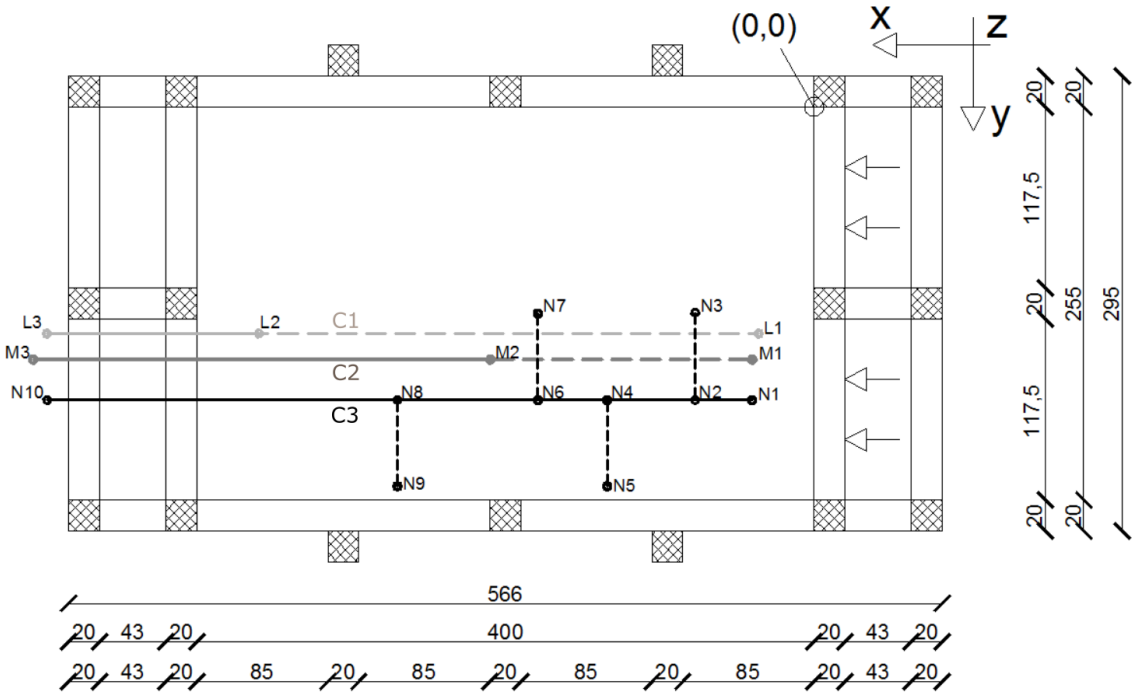

Figure S2. Ground plan of physical model with positions of pipes (karst conduits).

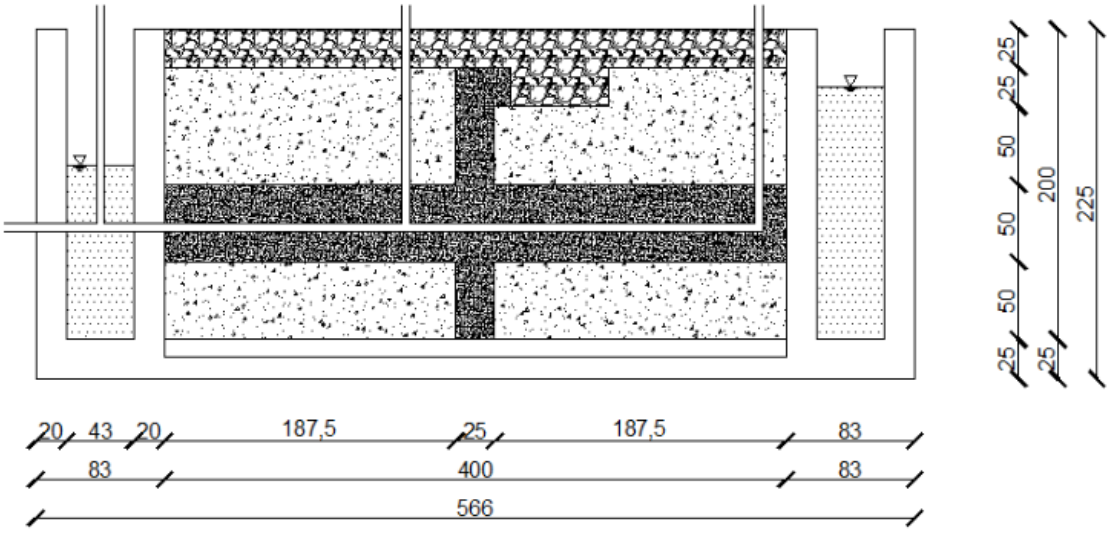

Figure S3. Cross section through conduit C2.

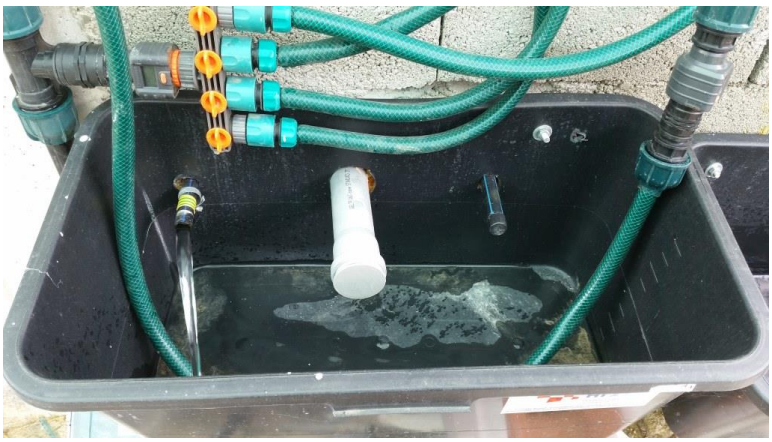

Figure S4. Photography of three conduit outlets.

Table S1. Coordinates of the conduit geometries.

COORDINATES	x [cm]	y [cm]	z [cm]
L1	36	147	75
L2	360	147	71.5
L3	497	147	70
M1	40	164	75
M2	210	164	73
M3	506	164	70
N1	40	190	75
N2	77	190	74.6
N3	77	134	74.6
N4	134	190	74
N5	134	246	74
N6	179	190	73.5
N7	179	134	73.5
N8	270	190	72.5
N9	270	246	72.5
N10	497	190	70

2.2. Distribution of materials

Three different types of the material are used: coarse quartz sand (CQS), fine quartz sand (FQS) and gravel (G). The material is filled in the eight layers of 25 cm with a different distribution of each material. In this manner, a certain level of heterogeneity in the matrix was achieved. Gravel is filled in the highest layer (eighth), and it represents a surface layer of epikarst. In the center part of the matrix, there is a fine quartz sand throughout the total cross-section as a weak permeable core. The same material is used around the conduits. as mentioned in the previous section. Tables S2-S3 and Figures S6-S13 present the details about the distribution of material.

Figure S5. Filling the material.

Table S2. Used materials.

MATERIAL	LABEL	SIZE RANGE [mm]	PERCENTAGE OF TOTAL VOLUME [%]
COARSE QUARTZ SAND	CQS	0-4	67.34
FINE QUARTZ SAND	FQS	0.1-0.6	13.98
GRAVEL	G	8-16	18.68

Table S3. Allocation of material.

	LAYER HEIGHT [cm]	**LAYER THICKNESS [cm]**	**MATERIAL TYPE AND DISTRIBUTION**		
			CQS [%]	FQS [%]	G [%]
Layer 1	0-25	25	11.69	0.81	-
Layer 2	25-50	25	10.76	0.81	0.93
Layer 3	50-75	25	7.54	4.34	0.62
Layer 4	75-100	25	6.89	4.34	1.27
Layer 5	100-125	25	9.48	0.92	2.10
Layer 6	125-150	25	10.89	0.81	0.80
Layer 7	150-175	25	10.10	1.94	0.46
Layer 8	175-200	25	-	-	12.5

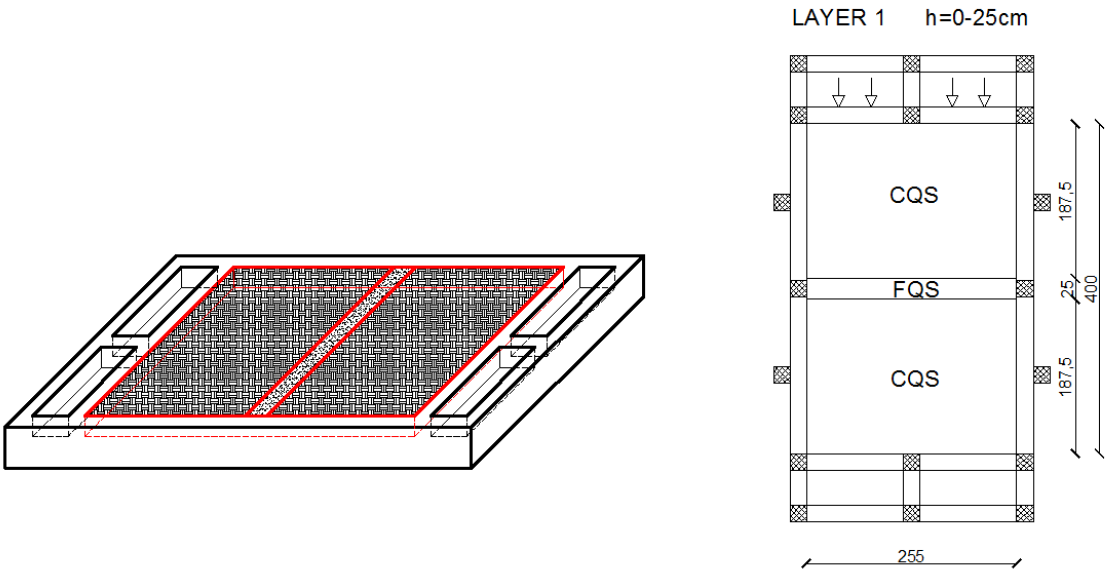

Figure S6. Schematic representation of layer 1.

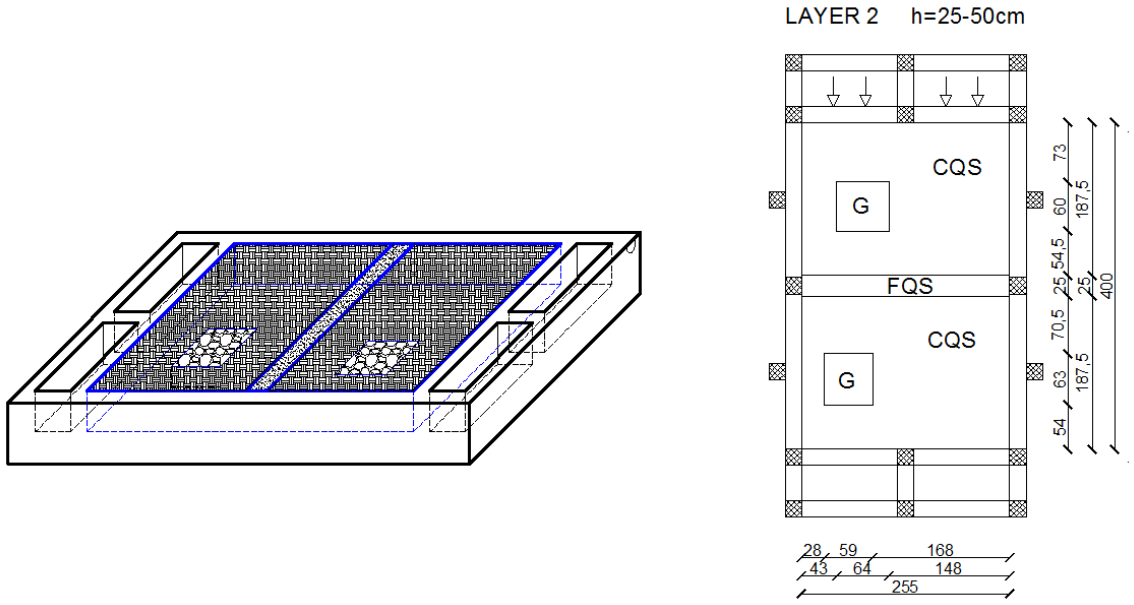

Figure S7. Schematic representation of layer 2.

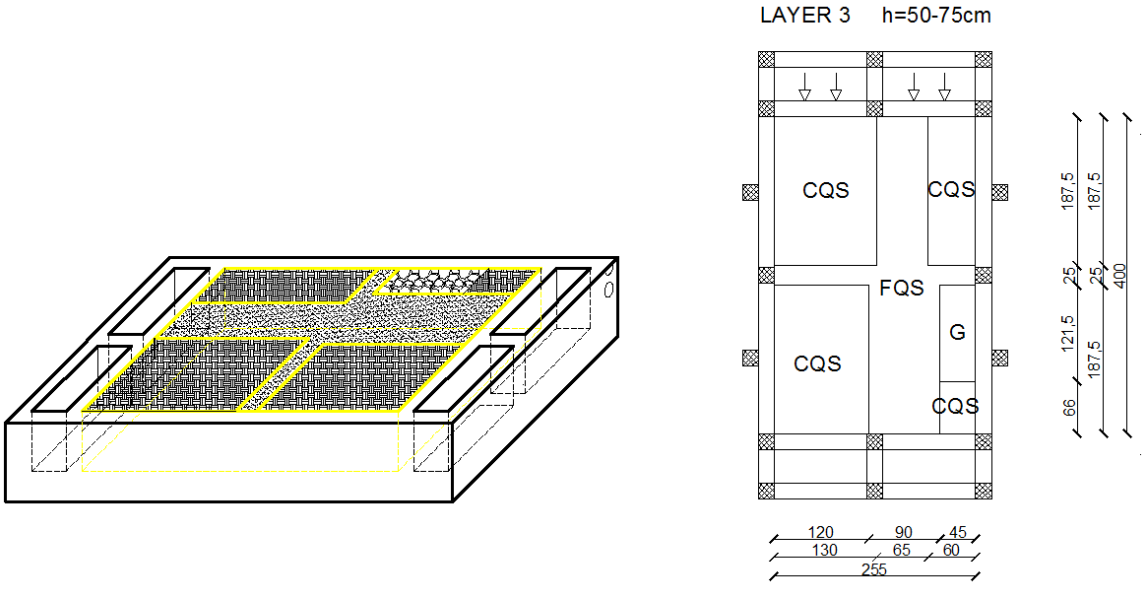

Figure S8. Schematic representation of layer 3.

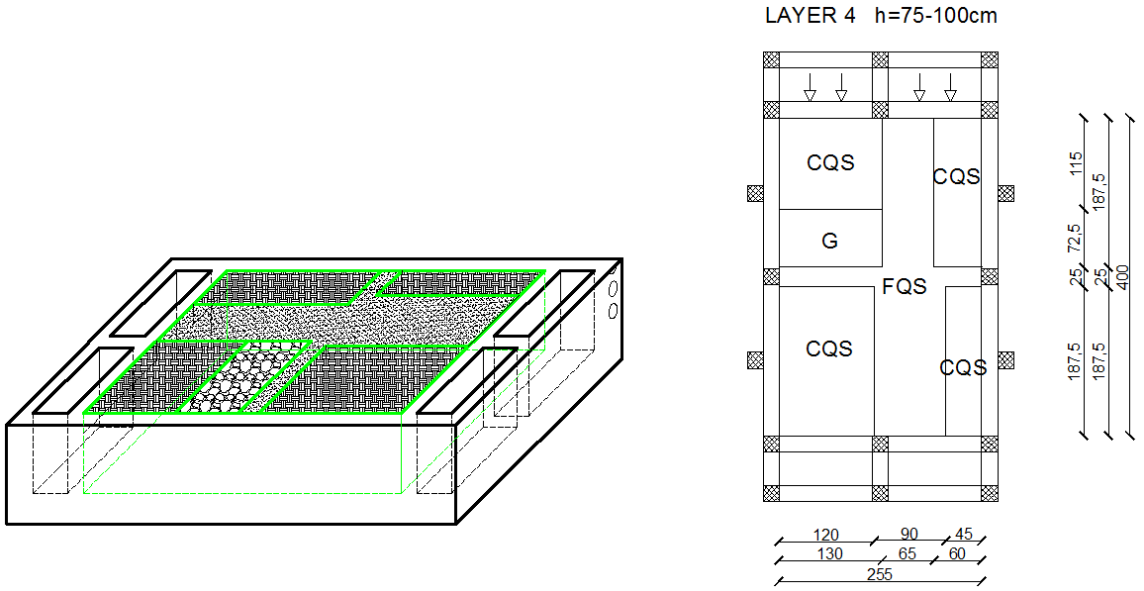

Figure S9. Schematic representation of layer 4.

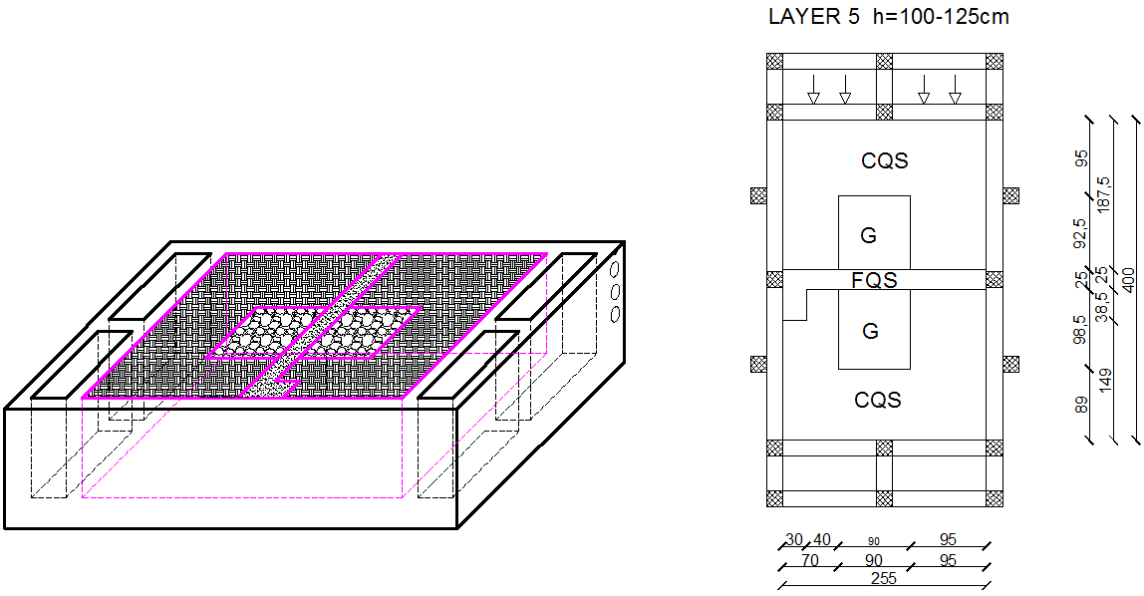

Figure S10. Schematic representation of layer 5.

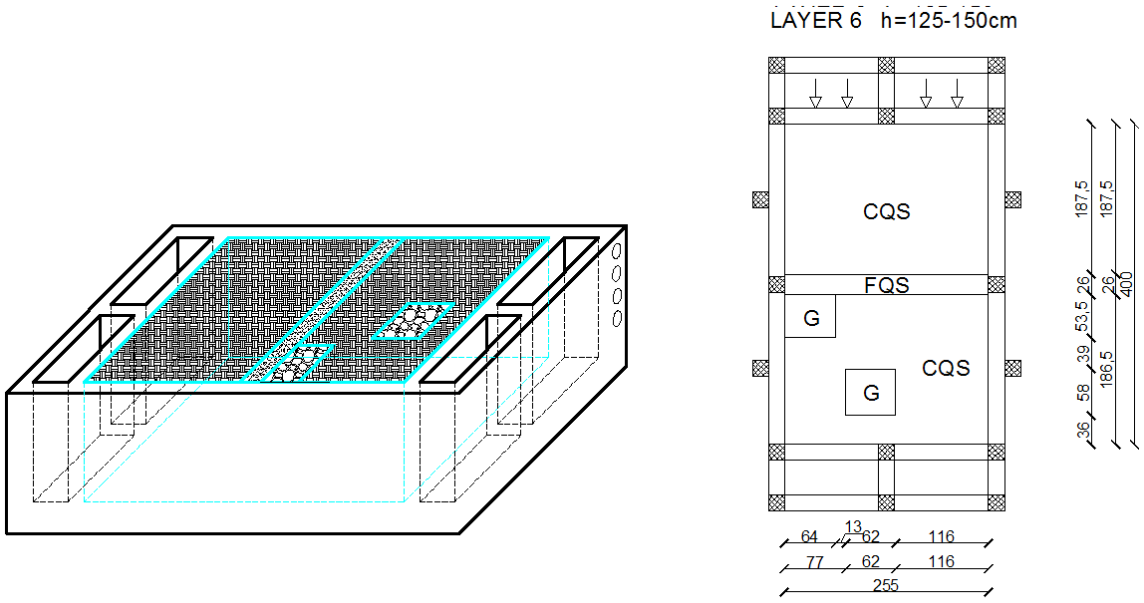

Figure S11. Schematic representation of layer 6.

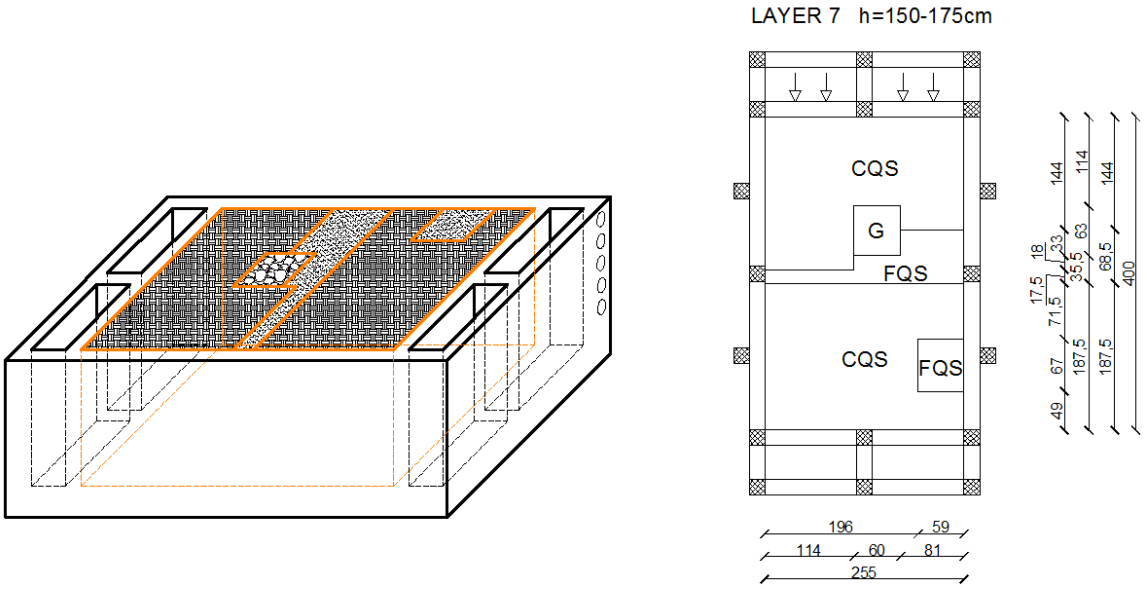

Figure S12. Schematic representation of layer 7.

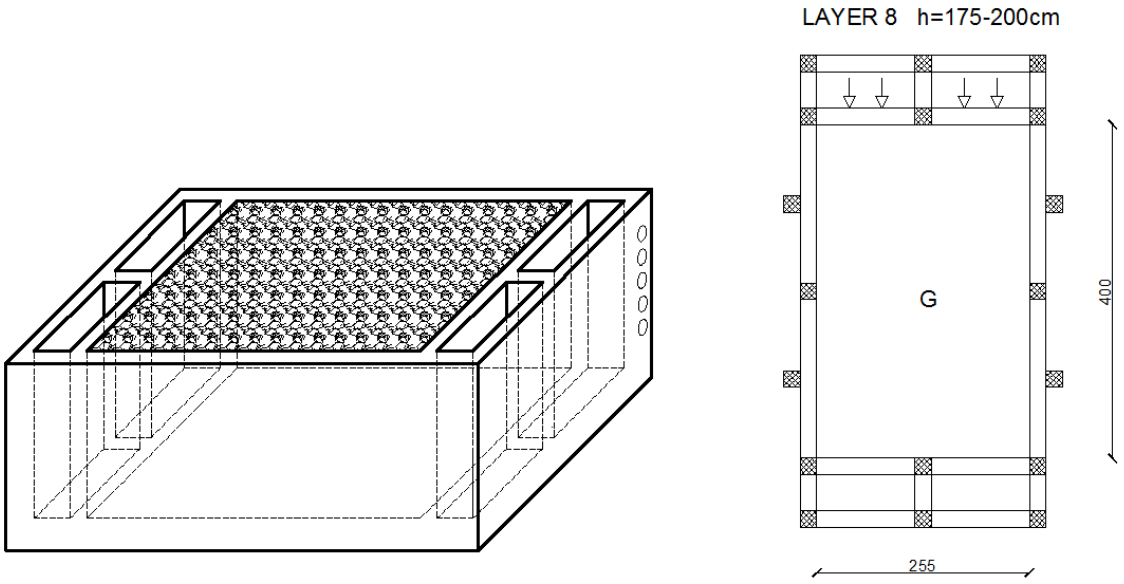

Figure S13. Schematic representation of layer 8.

2.3. Soil properties

The soil samples were sent to a specialized laboratory for the measurements of saturated and unsaturated soil parameters. However, because of extremely high conductivity, the results for gravel (G) were not obtained. Therefore, in addition to the obtained values in the laboratory (for CQS and FQS), the Darcys experiments were performed for all three materials. Then numerical calibration was performed on additional experiments (presented in section 3) to obtain final values. During numerical calibrations, there was a need to account for soil anisotropy to obtain reasonable results. Table S4 presents the obtained ranges and final values for saturated hydraulic conductivities. The specific storage coefficient (S_s) values were taken from the literature.

Table S4. Hydraulic conductivities: measured range and final values after calibration.

	Measurement range		Final value	
Material	K_{min} [m/s]	K_{max} [m/s]	K_H [m/s]	K_V [m/s]
CQS	$4.14 \cdot 10^{-4}$	$8.00 \cdot 10^{-3}$	$3.40 \cdot 10^{-3}$	$1.26 \cdot 10^{-3}$
FQS	$7.12 \cdot 10^{-5}$	$3.47 \cdot 10^{-4}$	$2.00 \cdot 10^{-4}$	$8.00 \cdot 10^{-5}$
G	$2.80 \cdot 10^{-2}$	$7.10 \cdot 10^{-2}$	$6.00 \cdot 10^{-2}$	$6.00 \cdot 10^{-2}$

Unsaturated soil properties are described by water retention curves. These curves present the relationship between soil suction and volumetric water content and are shown for three used materials in Figure S14. The measured values (for CQS and FQS) are fitted by the bimodal van Genuchten model, while the classical (unimodal) curve for G is obtained by the literature guidelines and numerical calibration. The values of the van Genuchten parameters are given in Table S5.

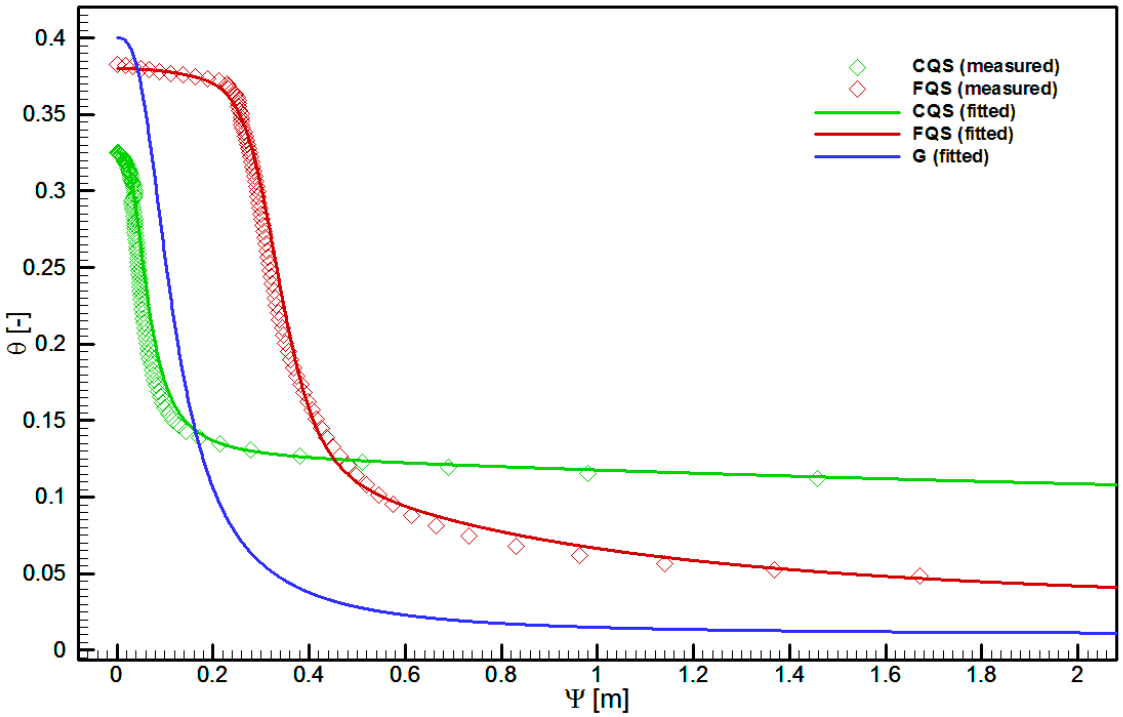

Figure S14. Water retention curves for used materials.

Table S5. Unsaturated soil parameters for three different materials: coarse quartz sand (CQS), fine quartz sand (FQS) and gravel (G).

	CQS	FQS	G
α_1 [m^{-1}]	18.00	3.00	10.00
α_2 [m^{-1}]	0.50	2.00	-
n_1 [-]	3.2	9.2	2.9
n_2 [-]	1.3	2.2	-
w_1 [-]	0.62	0.67	1.0
w_2 [-]	0.38	0.33	0.0
τ [-]	2.96	2.295	0.5
η [-]	0.325	0.38	0.40
θ_r [-]	0.005	0.02	0.01

2.4. Rainfall simulation

On the top of the model, there are sprinklers and shower heads for rainfall simulation. The sprinklers are used for rainfall simulation over total "epikarst" area, while shower heads produce high-intensity concentrated rainfall. There are two digital flowmeters for the measurement of total discharge from both rainfall components. These discharges are not perfectly uniform distributed over the considered area, but for the simplification of the numerical modeling their distribution is considered uniform. Figure S15 shows a picture of the rain simulation.

Figure S15. Photography of rain simulation by two shower heads.

2.5. Water regulation in reservoirs

The water levels in the reservoirs are regulated by height-adjustable overflows (Figures S16 and S17). The large perimeters were used to prevent water elevations during rainfalls and high pumping discharge rates (needed for circulation of water).

Figure S16. Overflow in upstream reservoir.

Figure S17. Overflow in downstream reservoir.

2.6. Discharge measurements

In order to make sense of the experiments, it is necessary to have accurate measurements of the flow from matrix and the conduits. The matrix discharge is regarded as total water that flows out from soil inside downstream reservoir. Since the reservoir level is fixed by high capacity overflow, the

matrix discharge is equal to overflow discharge. The reservoir overflow water (matrix discharge) and conduit outflow are directed toward two V-Notch weirs that are used as measurement devices (Figure S18). Each of them has a previously calibrated discharge scale (as function of water level inside weir box), and a camera is used to record the flow rates at given time intervals (see section 2.9). For large and fast changes in discharge (such as sudden opening of conduit), there is smoothing (time lag) in the measurements. Since different discharges are realized for different water levels, the filling/emptying of this volume of water is the main reason for this time lag. This time lag is estimated less than 1 min for maximum discharge variations used in the experiments.

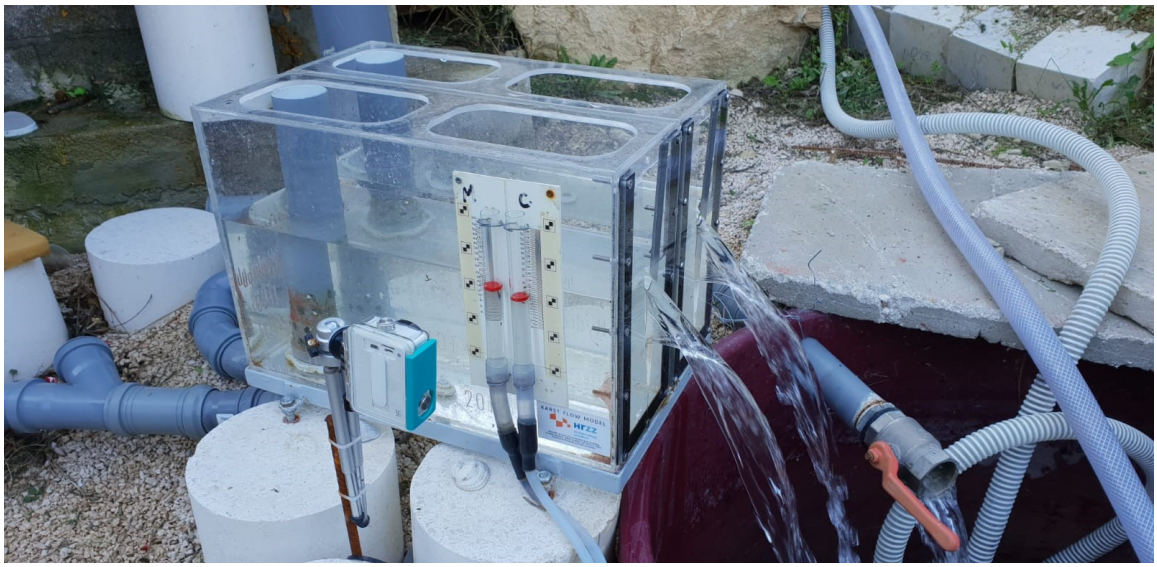

Figure S18. V-Notch weirs for discharge measurment.

2.7. Piezometers

Pressure distribution is measured in 44 fixed points by piezometers that are installed through the foundation slab and rise vertically (Figure S19). These pipes are perforated only on their ends (inside the porous medium) and connected with transparent tubings (level gauges) on front side of model (Figure S1). Water levels in this tubes represent head values in particular points inside the domain, and a camera is used to record the head variations at given time intervals (see section 2.9). Figure S20 shows the position of all installed piezometers, while their coordinates are given in Table S6. Some piezometers are shown to be malfunctioning and excluded from measurements, probably because of entrapped air or perforations clogging. The following is a list of piezometers that were not used: A11, B8, C9, C10, D2, D9 and D10.

Figure S19. Installation of piezometers.

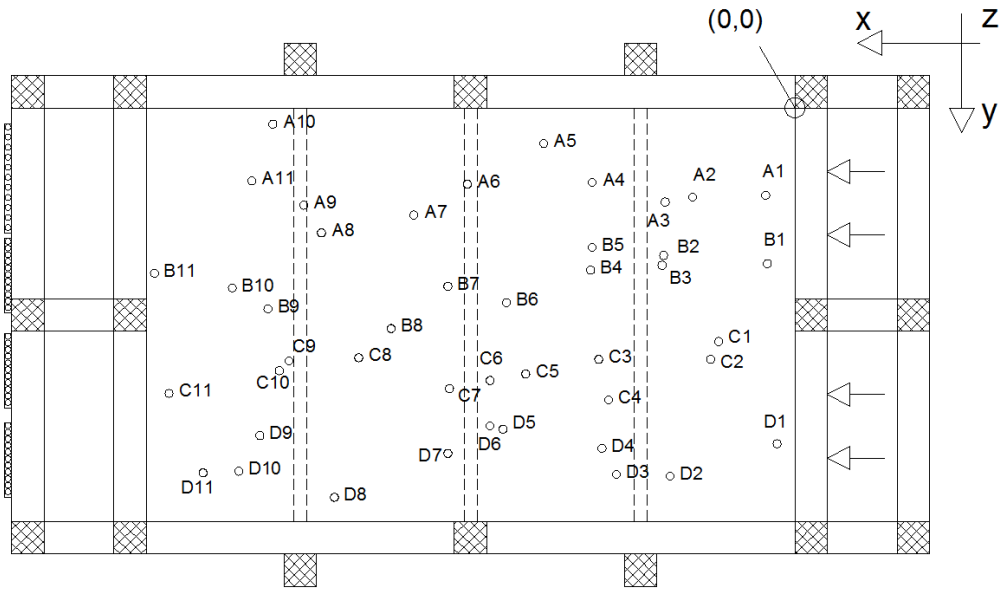

Figure S20. Positions of piezometers.

Table S6. Coordinates of the piezometers.

PIEZOMETER	x [cm]	y [cm]	z [cm]	PIEZOMETER	x [cm]	y [cm]	z [cm]
A1	17	54	77	C1	47	144	105
A2	63	54	100	C2	52	155	33
A3	80	58	32	C3	121	155	65
A4	125	46	75	C4	115	180	95
A5	155	22	100	C5	166	164	39
A6	202	47	42	C6	188	168	65
A7	235	66	65	C7	203	173	102
A8	292	77	106	C8	269	154	31
A9	303	60	33	C9	318	162	60
A10	322	10	100	C11	386	176	33
A11	335	45	70	C10	312	156	100
B1	17	96	33	D1	11	207	33
B2	81	91	65	D2	77	227	70
B3	82	97	100	D3	110	226	100
B4	126	100	33	D4	117	210	34
B5	125	86	65	D5	180	198	69
B6	178	120	100	D6	188	196	120
B7	216	110	43	D7	214	213	36
B8	249	136	60	D8	284	240	60
B9	325	124	100	D9	330	202	100
B10	347	111	33	D10	343	224	34
B11	395	102	60	D11	365	225	85

2.8. Boreholes

The 25 fully perforated vertical pipes are installed from soil surface, and they are denoted as boreholes. Since these pipes are fully perforated, borehole packers (Figure S21) are used to isolate part of pipe (approximately 10 cm) on the specific depth. The pressure sensor or water hose can be installed at any depth of the borehole and used for pressure measurements or performing partially penetrating pumping tests, respectively. Figure S22 shows the positions of all installed boreholes, while their coordinates are given in Table S7.

Figure S21. Borehole pakers.

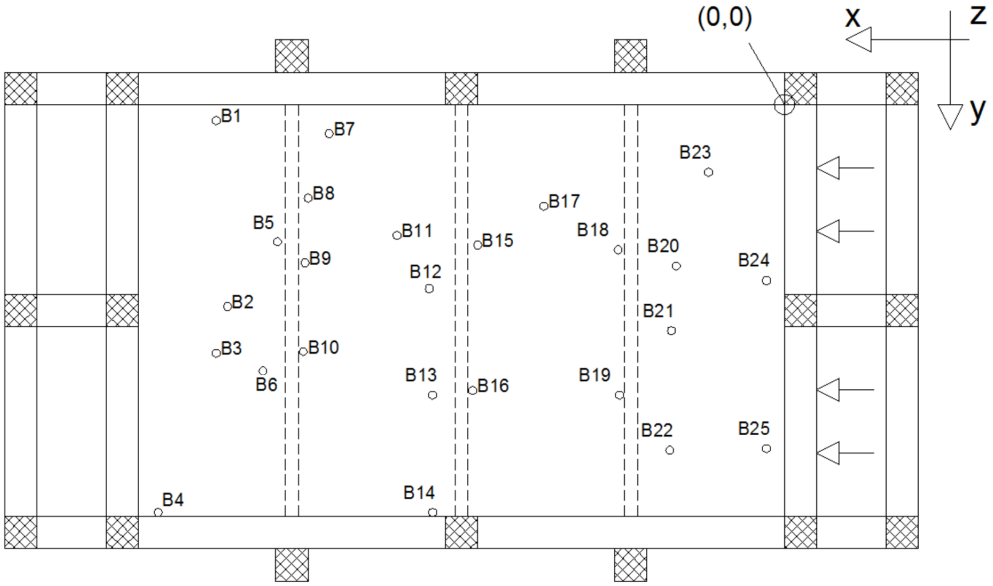

Figure S22. Borehole positions.

Table S7. Coordinates of the boreholes.

BOREHOLE	x [cm]	y [cm]	BOREHOLE	x [cm]	y [cm]
B1	353	10	B14	219	254
B2	345	124	B15	196	87
B3	352	154	B16	204	172
B4	388	255	B17	150	58
B5	314	85	B18	105	90
B6	318	166	B19	103	177
B7	282	17	B20	75	105
B8	296	58	B21	76	184
B9	298	97	B22	84	209
B10	299	153	B23	53	42
B11	241	76	B24	9	109
B12	236	110	B25	8	213
B13	230	174	-	-	-

2.9. Photogrammetric tracking

Considering the large numbers of level gauges employed during the experiment (Figure S23), experiment length, and low temporal constant of the measured system, photogrammetry was used as an inexpensive and robust measurement method. For image acquisition, an inexpensive wide-angle sports camera was used. The fixed aperture of the camera was f/2.8 with a focal length of 3 mm. The camera was mounted 1 m from level gauge panel, with optical axis horizontal and perpendicular to measurement plate. An additional camera, with the same parameters, was used to monitor flow rate. Image acquisition was automatic, relying on an integrated time-lapse mode. The interval of time-lapse was 5 s.

The data acquisition process from images was semiautomatic. Initially, the operator was defining curvilinear tracks that were aligned with the optical path of level gauges and curvilinear levels that were defined according to height marks plotted onto the measurement plane. These two sets of curves defined the prescribed paths of level gauge knobs and actual, physical world water levels. There was

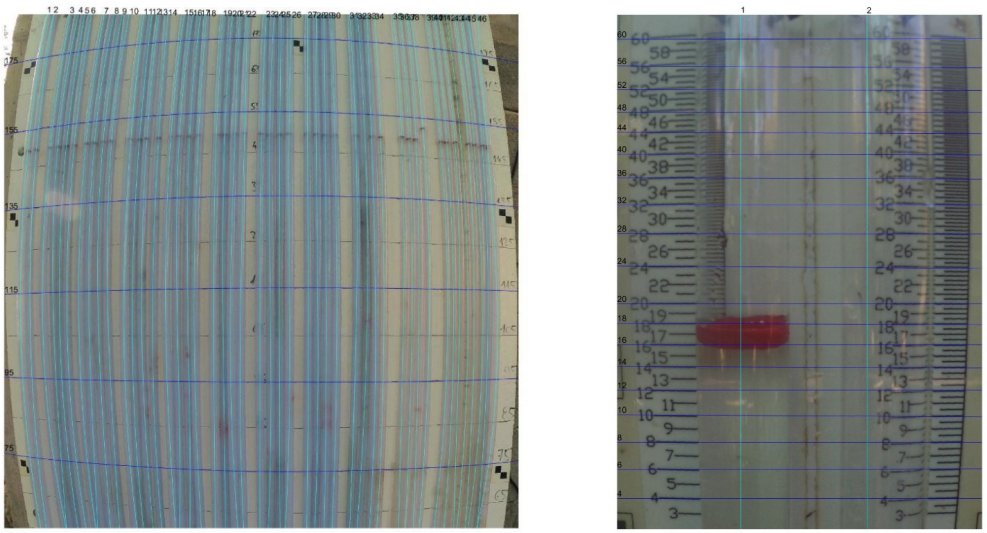

(a) Piezometric head scale **(b)** Discharge scale

Figure S23. Curves defining paths along water height level (cyan) and curves defining levels (blue). Buoy for water level detection are red blobs.

no need for the rectification of photographs since the described method introduced corrections via curvilinear coordinates. The curves used to describe paths and levels were polynomial expressions (independent variable x (horizontal) for level curves and independent variable y (vertical) for path curves). The detection of a buoy inside was based on the difference in color regarding the level gauge background. Along each track, a 5 pixel strip on both sides of the track was taken into account. The collected pixel strip was squarely differentiated with buoy color vector and averaged both over 11-pixel span and three components of the color resulting 1D plot of the most likely position of buoy along the track. In order to minimize color variations between frames due to reflections and changes in natural lighting, histogram matching was performed before the definition of the buoy position. The detected position was the mean of the 1D plot. After detection, the pixel position of the buoy was translated to the water level using the interpolation of pixel positions of the intersection of specified track and level lines and water column height (Figure S24).

After initiation, the procedure is automated for each frame. The primary sources of error were due to rotation of buoys and image space nonlinearities. The rough mistakes were corrected by operators after completed data acquisition, and systemic mistakes were taken into account as measurement uncertainties. The number of rejected measurements were dependent on the track position and optical opaqueness of the water-level column tube, but usually less than 5% of all measurements. Typical error of measurement was 1.5 cm for the water-level column and 1 l/s for flow rate measurement. The measurement errors were proven by using additional concurrent measurements of the stated properties as a benchmark.

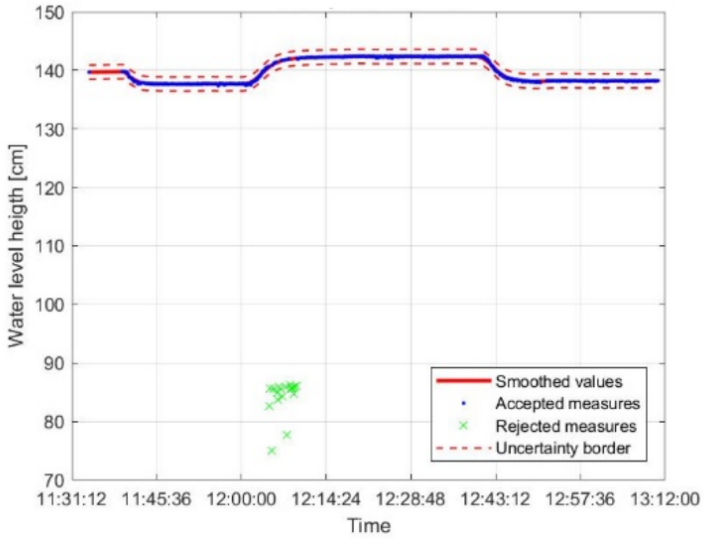

Figure S24. Typical measurements output, depicting accepted values, rejected values, smoothed output and error boundary.

3. Additional experiments

In the following we briefly describe additional experiments used for calibration of hydraulic conductivities. The full experimental data for additional experiments, together with two test cases from the article, are available online.

Seven (E01-E07) steady-state flow experiments were performed (Table S8). First four experiments (E01-E04) consider only matrix flow, since all three conduit systems were clogged. The borehole packers were used to perform partially penetrating pumping tests, while the difference between water levels in two reservoirs was practically negligible (0.003 m) to produce similar hydraulic gradients in both horizontal and vertical directions. Boreholes B11, B12, B13 and B17 (see Figure S22) were used and similar pumping discharge was applied at different depths.

The remaining three experiments (E05-E07) were used to test conduit influence on matrix steady-state flow. The head difference in two reservoirs is unchanged and set $\Delta H = 0.165$ m. The experiment E05 considers only matrix flow, whereas E06 and E07 consider matrix interaction with conduits C1 and C2, respectively. The discharges and hydraulic head values in piezometers were measured after conduit-matrix steady-state was achieved.

Table S8. Description of additional experiments.

Experiment ID	$H_{upstream}$ [m]	$H_{downstream}$ [m]	$Q_{recharge}$ [l/min]	Borehole	Packer depth [m]	Active conduit
E01	1.455	1.452	32.30	12	0.74	-
E02	1.455	1.452	32.40	13	0.87	-
E03	1.455	1.452	33.30	17	0.87	-
E04	1.455	1.452	32.20	11	0.62	-
E05	1.455	1.290	0.00	-	-	-
E06	1.455	1.290	0.00	-	-	C1
E07	1.455	1.290	0.00	-	-	C2

Funding: This research was funded by the Croatian Science Foundation (in Croatian Hrvatska zaklada za znanost - HRZZ) through grant number: UIP-2013-11-8103).

Acknowledgments: We thank our colleagues, Dr. Sc. Mijo Vranjes and our technician Kresimir Vranjes for valuable help related to physical model..